PHYSICAL REVIEW B **72**, 235313 (2005)

Structural, electrical, and magneto-optical characterization of paramagnetic GaMnAs quantum wells

M. Poggio, R. C. Myers, N. P. Stern, A. C. Gossard, and D. D. Awschalom

Center for Spintronics and Quantum Computation, University of California, Santa Barbara, California 93106, USA

(Received 18 March 2005; revised manuscript received 20 July 2005; published 12 December 2005)

The growth of GaMnAs by molecular beam epitaxy is typically performed at low substrate temperatures (~250 °C) and high As overpressures, leading to the incorporation of excess As and Mn interstitials, which quench optical signals such as photoluminescence (PL). We report on optical-quality $Ga_{1-x}Mn_xAs/Al_{0.4}Ga_{0.6}As$ quantum wells (QWs) with $x < 0.2\%$ grown at a substrate temperature of 400 °C. Electrical and structural measurements demonstrate that this elevated temperature reduces As defects while allowing the substitutional incorporation of Mn into Ga sites. From a combination of Hall and secondary ion mass spectroscopy measurements we estimate that at least 70%–90% of the Mn incorporates substitutionally in all samples studied. The incorporation behavior shows both a substrate temperature and QW width dependence. The low defect density of these heterostructures, compared to typical lower-temperature-grown GaMnAs, enables the observation of both polarization-resolved PL and coherent electron spin dynamics, from which the conduction-band exchange parameter is extracted. No evidence of long-range Mn spin coupling is observed, whereas negative effective Curie temperatures indicate spin heating due to photoexcitation. Light Mn doping maximizes the electron spin lifetime, indicating the importance of the Dyakonov-Perel decoherence mechanism in these structures. PL spectra reveal a low-energy peak from shallow donors, which, because of the paramagnetic behavior of its PL polarization, we ascribe to Mn interstitials.

DOI: 10.1103/PhysRevB.72.235313 PACS number(s): 71.70.Gm, 75.50.Pp, 78.47.+p, 61.72.Vv

I. INTRODUCTION

Since the invention of the ferromagnetic semiconductor $Ga_{1-x}Mn_xAs$, by Ohno *et al.*,[1] it has been the subject of intense experimental work. The combination of electronic and magnetic properties in this system has enabled many interesting experimental demonstrations arising from the carrier-mediated nature of its ferromagnetism,[2] which provides an excellent test bed for semiconductor spintronics since the host material system is a highly engineered optoelectronic semiconductor.[3,4] As a consequence of both the low solubility of Mn in GaAs and the high concentrations of substitutional Mn (Mn_{Ga}) required for ferromagnetism to occur (~5%, ~10^{21} cm^{-3}), molecular beam epitaxy (MBE) growth at present is performed at low substrate temperatures (~250 °C) and high arsenic overpressures. This is a regime of growth in which defects, chiefly excess As and Mn interstitials (Mn_i), are incorporated into the epilayers at concentrations that quench sensitive optical properties, such as photoluminescence (PL) and absorption. These optical properties can provide direct measurements of the energy splitting for spin-up and spin-down carriers at the band edges. In II-VI dilute magnetic semiconductors (DMS), for example, polarization-resolved magneto-PL or absorption has been used to extract the exchange constants.[5] The ability to perform such optical measurements in GaMnAs is an important step in understanding the exchange interactions in this material.

Polarization-resolved PL spectroscopy is a useful tool for the measurement of conduction- and valence-band spin splittings in magnetic fields. PL techniques including measurements of the exciton Zeeman splitting, the Hanle effect, and the PL decay time have been used to determine electron and hole g factors in semiconductor heterostructures.[6–8] Additionally, the measurement of Kerr rotation (KR) or Faraday rotation (FR) serves as an extremely sensitive probe of magnetization, resolving fewer than ten electron spins in bulk GaAs.[9] This technique has led to a variety of advances in nonmagnetic GaAs-based heterostructures including the electrical tuning of the g factor,[10–12] observation of the strain-induced spin-orbit interaction,[13,14] and the measurement of the spin-Hall effect.[9] In addition to electron spin dynamics, the technique has been used to measure magnetic ion spin coherence in II-VI ZnCdSe/MnSe quantum structures[15] and, recently, in experiments demonstrating electrical control of the exchange-enhanced electron spin splitting.[16] The growth of optical-quality GaMnAs allows for the application of the aforementioned techniques and opens the door to a variety of measurements including the precise determination of the s-d (p-d) exchange parameter $N_0\alpha$ ($N_0\beta$) between electron spins in the s-like conduction (p-like valence) band and the 3d spins localized on Mn^{2+}. From a practical standpoint, long electron spin lifetimes and compatibility with previously developed heterostructures for electron spin control favor the development of magnetically doped devices in GaAs-based III-V materials.

The purpose of this work is to develop the capability to grow GaMnAs structures by MBE in which coherent spin dynamics can be observed optically. Preliminarily, our growth campaign focused on achieving stoichiometric GaMnAs grown at a typical low temperature of 250 °C, at which the use of As overpressures leads to large concentrations of excess As. Stoichiometric growth can be achieved at low substrate temperatures by digital growth techniques, such as atomic layer epitaxy (ALE) in which the As flux is shutter controlled[17] or analog growth in which the As flux is controlled by source temperature and/or valve position. The former technique has enabled digital ferromagnetic heterostructures made up of submonolayers of MnAs with independent control of charge carriers in the nonmagnetic GaAs spacer layers, while hybrid growths using both high-temperature MBE (optical layer) and low-temperature ALE (magnetic layer) have been developed to enable optical quality in GaAs-AlGaAs quantum wells (QWs) with a ferromagnetic barrier.[18] Although polarization-resolved PL from these QWs demonstrates a spin coupling between the magnetic layer and carriers in the QWs, no time-resolved KR could be measured. In previous work using the As valve for flux control, it was found that stoichiometric GaAs grown at 250 °C could be achieved as indicated by the low charge compensation of doped carriers (1×10^{16} cm^{-3}); however, the incorporation of Mn at levels required for ferromagnetism could only be achieved by using an As overpressure. The resulting defects quenched both PL and time-resolved KR signals.[19] In the current work we investigate MBE-grown GaMnAs/AlGaAs QWs with low Mn-doping levels ($x<0.2\%$). At these Mn concentrations the substrate temperature can be increased to 400 °C while allowing substitutional incorporation of Mn. In contrast to low-temperature stoichiometric growth, at the increased growth temperatures used here an As overpressure does not result in excess As incorporation, enabling the observation of PL and time-resolved electron spin dynamics in GaMnAs QWs.

Here we discuss structural, electrical, and magneto-optical properties with respect to the growth conditions and incorporation behavior of Mn in GaMnAs QWs. The effect of the substrate growth temperature (T_{sub}) on the incorporation of Mn is studied by secondary-ion mass spectroscopy (SIMS) measurements of the Mn concentration profiles (Sec. III). The activation energy for Mn acceptors in the QWs is found by measuring the hole concentrations as a function of temperature using the Hall effect (Sec. IV). Comparison between the SIMS and Hall data allows us to estimate the fraction of Mn$_{Ga}$ acceptors incorporated in the QWs assuming that hole compensation is dominated by Mn$_i$ donors (Sec. V). Time-resolved KR measurements indicate that Mn doping at $<10^{19}$ cm^{-3} maximizes the electron spin lifetime. These data show evidence for spin heating due to photoexcitation and no long-range Mn spin coupling. The electron spin splitting increases with magnetic doping, allowing for the determination of the conduction-band exchange constant $N_0\alpha$ (Sec. VI). This has led to the surprising observation in GaMnAs QWs of an antiferromagnetic $N_0\alpha$, whose dependence on QW width indicates a contribution from kinetic exchange due to the confinement energy of the QW.[20] Last, we discuss the polarization-resolved PL of the QWs in which the low-energy peak is attributed to the bound exciton emission from Mn$_i$ donors (Sec. VII). The polarization of this PL is proportional to the magnetization of Mn$_i$ within the QWs, providing an indirect optical readout of magnetic moments within the QWs.

II. GROWTH

Samples are grown on GaAs substrates in a Varian GEN-II MBE system manufactured by Veeco Instruments, Inc. In corroboration with the recent findings of Wagenhuber *et al.*,[21] we find that the inclusion of Mn growth capability in the MBE system does not preclude the growth of high-mobility samples. We have measured low-temperature mobilities greater than 1.7×10^{6} cm^2/(V s) in typical modulation Si-doped AlGaAs/GaAs two-dimensional electron gas structures grown in our chamber at 630 °C. For Mn-doped QWs, however, we use a lower growth temperature to enable the substitutional incorporation of Mn. Samples are grown at 400 °C as monitored and controlled during growth by absorption band-edge spectroscopy (ABES) using white-light transmission spectroscopy through the substrate, providing a typical substrate temperature stability of ±2 °C. The growth rate of GaAs is ~0.7 ML/s and of Al$_{0.4}$Ga$_{0.6}$As is ~1 ML/s as calibrated by reflection high-energy electron diffraction (RHEED) intensity oscillations of the specular spot. The As$_2$:Ga beam flux ratio for all samples is 19:1 as measured by the beam equivalent pressure of each species using a bare ion gauge in the substrate position. Mn cell temperatures for doping were extrapolated from growth rate calibrations of MnAs measured at much higher growth rates using RHEED oscillations; the actual, measured, value of Mn-doping concentrations is discussed in detail in later sections.

The QWs, shown schematically in Fig. 1(a), are grown on (001) semi-insulating GaAs wafers using the following procedure. The substrate is heated to 635 °C under an As overpressure for oxide desorption and then cooled to 585 °C. With the substrate rotating at 10 rpm throughout the growth, a 300-nm GaAs buffer layer is first grown using 5-s growth interrupts every 15 nm for smoothing, which results in a streaky 2×4 surface reconstruction pattern as observed by RHEED. A 500-nm layer of Al$_{0.4}$Ga$_{0.6}$As is grown followed by a 20-period digital superlattice of 1 nm AlAs and 1.5 nm GaAs. The sample is then cooled to the growth temperature (usually 400 °C, but also 350 and 325 °C) during which the RHEED pattern changes to a 4×4 reconstruction. The first QW barrier consists of a 50-nm Al$_{0.4}$Ga$_{0.6}$As layer; during its growth the 4×4 pattern becomes faint and changes to 1×1. Before the QW layer, a 10-s growth interrupt is performed to smooth the interface; during this wait the RHEED partially recovers a 4×4 reconstruction pattern. The GaMnAs QW layer deposition causes the 4×4 to again become faint, leading to 1×1, but during the next 10-s wait on the top side of the QW, a 4×4 partially recovers. Increased Mn doping leads to surface roughening as evidenced by the development of a spotty RHEED pattern during and after the QW growth. In contrast, lower-doped samples, which emit PL and show time-resolved KR signal, display a streaky two-dimensional RHEED pattern throughout their growth. The structure is completed by a top QW barrier of 100-nm Al$_{0.4}$Ga$_{0.6}$As and a 7.5-nm GaAs cap after which a streaky 4×4 reconstruction pattern is observed.

III. SECONDARY-ION MASS SPECTROSCOPY

A. Manganese-doping profiles

The Mn concentration profile for each sample is measured using SIMS[22–24] and is plotted in Fig. 1(b) for a set of four 7.5-nm QWs grown on the same day at 400 °C with differ-

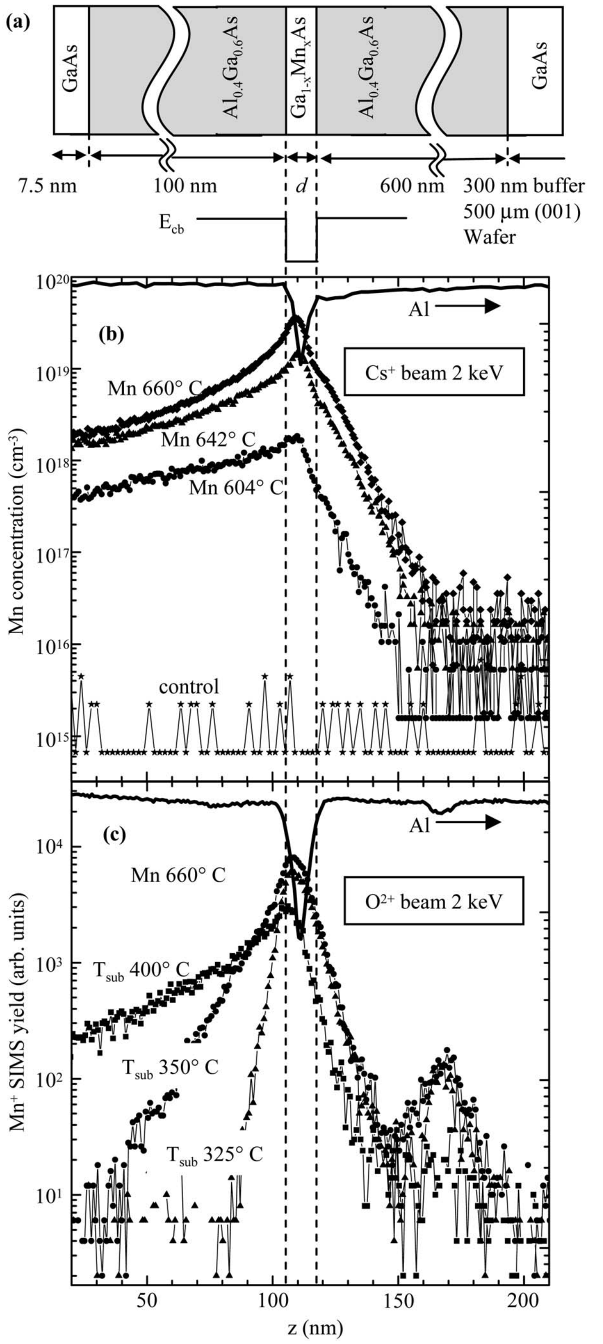

FIG. 1. (a) Schematic of sample layer structure and conduction-band energy along the growth axis $\hat{z}$. (b) Mn concentration profile measured by SIMS for four 7.5-nm QWs with varying Mn-doping level (Mn effusion cell temperatures marked in the figure) and (c) for QWs with the same Mn-doping level but varying substrate temperatures (marked in the figure). The uncalibrated Al SIMS signal (plotted as black lines) serves as a marker for the QW region.

ent Mn-doping levels. The primary beam consists of Cs^+ ions with an impact energy of 2 keV providing a depth resolution of 3.25 nm/e, as calibrated using the atomically sharp AlGaAs/GaAs interface as a reference. The secondary ion used to measure the Mn concentration is $CsMn^+$, which is resilient to changes in ionization yield at the AlGaAs/GaAs interface. The calibration of the SIMS Mn signal was performed using Mn-ion-implanted GaAs as a reference, while the change in ionization yield of $CsMn^+$ between AlGaAs and GaAs was checked using Mn-ion-implanted AlGaAs reference samples. The z-axis calibration for the SIMS scans was performed using the Al signal as a reference for the QW region as well as the lower edge of the barrier, both layers grown at low temperature. The depth of the crater could not be used to calibrate the z axis since it was found that the low-temperature-grown layers sputter faster than the high-temperature-grown buffer layers.

The Mn concentration peaks near the center of the QW region, as expected, but the surface side of the QW shows a large residual concentration of Mn which is incorporated into the structure even after the Mn shutter has closed. Such behavior is not unexpected, even if the Mn-doping concentration is below the equilibrium solubility limit, since the growing surface is not at equilibrium. This behavior has previously been reported for similar structures in which Mn δ-doped GaAs grown at 400 °C showed large surface segregation.[25] We note that our results do not agree quantitatively with those of Nazmul *et al.* and we attribute this discrepancy to the different methods used for substrate temperature measurement in these two studies, noting that Mn incorporation is highly sensitive to this growth parameter. In our MBE system, the substrate temperature is measured directly by ABES, while an indirect temperature reading from a radiatively coupled thermocouple, used by Nazmul *et al.* can be more than 50 °C from the actual substrate temperature.

Mn surface segregation during growth may lead to Mn clustering in our samples and allow second-phase magnetic precipitates, such as MnAs, to form. We note, however, that though these impurities are likely present in our samples, the Schottky barrier around such precipitates prevents their detection in the electrical or optical signal of free carriers in the quantum wells. In the next section, the hole conductivity and carrier densities measured in these samples indicate, in comparison with the SIMS data, that most of the Mn impurities present in the sample are substitutionally incorporated. Thus Mn surface segregation and related growth defects have a negligible effect on our optical studies of the exchange splittings.

Below the QW, the Mn concentration decreases toward the substrate, reaching a minimum point ~100 nm below the QW. The Mn profile is broader than the Al depth profile, indicating either a SIMS measurement artifact, such as poor depth resolution or preferential Mn sputtering—i.e., knock-on effects[26,27]—or that Mn diffuses into the barrier. The lack of any temperature or doping level dependence on the Mn profile below the QW eliminates the latter possibility, while Mn knock-on effect has been reported in similar structures grown by Nazmul *et al.* To test for the presence of the knock-on effect, we run SIMS scans on the same sample (C) at two different beam energies 2 keV and 8 keV, Fig. 2. Indeed, the Mn profile on the substrate side of the QW shows a beam energy dependence with a decay of 17 nm/e for 8 keV and 10 nm/e at 2 keV. The Mn tail on the surface side of the QW, where Mn incorporates as it floats along the surface, does not show any significant dependence on the beam energy. As a further test, we use an atomic force mi

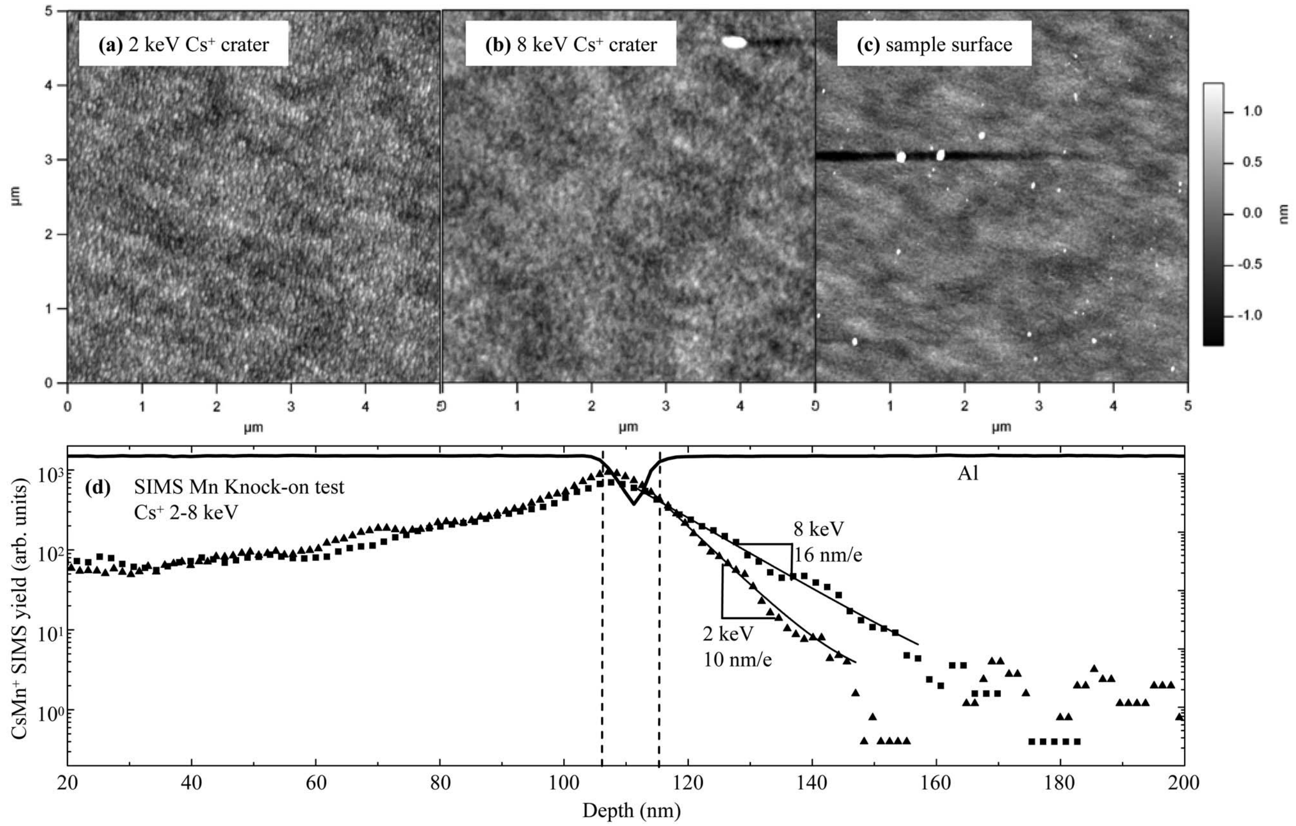

FIG. 2. Beam energy test for preferential Mn sputtering (knock-on). (a) and (b) show AFM images of the sample morphology in the center of SIMS craters formed by a 2-keV and 8-keV Cs^+ beam, respectively. (c) AFM image of the bare sample surface. (d) The Mn profiles in sample C measured at two different beam energies as labeled. Solid lines are exponential fits to the Mn profile tail below the QW.

+croscope (AFM) to measure the roughness of the SIMS craters for the 2-keV and 8-keV scans as 0.32 nm rms and 0.30 nm rms, respectively, while the roughness of the starting surface is 0.14 nm rms. Since the crater roughness does not depend on beam energy, we conclude that the sample is uniformly sputtered at these two beam energies. Therefore, the observed difference in decay of the Mn profile is a result of the knock-on effect. Thus, the Mn profiles on the substrate side of the QW are sharper than the SIMS data show.

After the lower Mn tail, ~100 nm below the QW, the Mn profile becomes constant for all samples. Though the value of this background Mn concentration is near the detection limit of SIMS, it is seen to scale with Mn cell temperature as seen in Fig. 1(b). This behavior suggests that Mn flux escapes from the hot Mn cell and is incorporated into the substrate even with the shutter closed. The Mn background for the control sample, grown with a cold Mn cell, is well below the SIMS detection limit.

B. Substrate temperature dependence

In Fig. 1(c), the Mn SIMS profiles are plotted for three 7.5-nm-wide QWs grown with the same Mn cell temperature (same Mn beam flux), but different substrate temperatures. These SIMS scans were performed using an O^{2+} 2-keV beam. Note that the Mn profiles measured with the O^{2+} beam show a large sensitivity to AlGaAs/GaAs interfaces, probably due to oxygen impurities incorporated during growth in the AlGaAs layers; thus, the vertical axis of these scans is uncalibrated (arbitrary units). The data, however, are qualitatively meaningful in the interface-free regions—e.g., the top QW AlGaAs barrier.

As the substrate temperature is decreased, the Mn concentration profiles become dramatically sharper, the surface tail is eliminated, and the peaks become taller, indicating that, as expected, the Mn incorporation is energetically more favorable at lower temperature. Sharp Mn profiles, particularly on the surface side of the QW, are desirable for the engineering of more complex magnetic quantum structures in which a precise control of the magnetic doping is required. Optical signals, however, even at the relatively high growth temperatures of 325 and 350 °C, quench due to increased defect densities even in the nonmagnetic control samples. Preliminary work shows that optical-quality nonmagnetic and magnetically doped InGaAs/GaAs QWs can be grown at 350 °C, suggesting that the loss in signal for the GaAs/AlGaAs QWs is related to Al, well known for its impurity gettering of oxygen defects during MBE growth.[28,29] Also noteworthy is a secondary peak in the Mn concentration 50 nm below the QW that occurs only in the 325 °C- and 350 °C-grown samples. This Mn peak corresponds to the interface between the high-temperature- and low-temperature-grown QW barrier, a point at which a long growth pause takes place. The peak indicates that the closed-shutter Mn

TABLE I. Quantum well substrate growth temperature (T_{sub}), width (d), room-temperature hole density (p), Mn concentration (Mn), x, p/Mn, estimated fraction of substitutional Mn (Mn_{Ga}/Mn), and activation energy of holes (E_a).

Sample	T_{sub} (°C)	d (nm)	p (cm^{-3})	Mn (cm^{-3})	x(%)	p/Mn	Mn_{Ga}/Mn	E_a (meV)
A	400	7.5	1.02×10^{18}	1.44×10^{18}	0.0065	0.71	0.90	68
B	400	7.5	2.13×10^{18}	1.19×10^{19}	0.0537	0.18	0.73	73
C	400	7.5	4.10×10^{18}	2.80×10^{19}	0.1266	0.15	0.72	96
D	400	3		5.50×10^{17}	0.0025		0.67	
E	400	3	1.62×10^{18}	2.60×10^{18}	0.0117	0.62	0.87	
F	400	3	3.37×10^{18}	6.06×10^{18}	0.0274	0.56	0.85	
G	400	10	9.58×10^{17}	2.97×10^{18}	0.0134	0.32	0.77	54
H	400	10	2.15×10^{18}	6.87×10^{18}	0.0310	0.31	0.77	41
I	400	10	3.89×10^{18}	1.78×10^{19}	0.0804	0.22	0.74	46
J	400	10	4.61×10^{18}	2.82×10^{19}	0.1274	0.16	0.72	59
K	400	5	4.59×10^{17}	9.65×10^{17}	0.0044	0.48	0.83	
L	400	5	1.47×10^{18}	2.43×10^{18}	0.0110	0.61	0.87	
M	400	5	3.11×10^{18}	7.03×10^{18}	0.0318	0.44	0.81	36
N	400	5	4.01×10^{18}	1.27×10^{19}	0.0574	0.32	0.77	47
O	350	7.5						
P	325	7.5						
Q	400	500	2.14×10^{18}	1.35×10^{19}	0.0610	0.16	0.72	71
R	400	500	6.86×10^{18}	6.25×10^{19}	0.2823	0.11	0.70	54
S	400	500	3.39×10^{18}	1.39×10^{20}	0.6292	0.02	0.67	53

flux, which scales with Mn cell temperature as discussed previously, may accumulate on the surface during the substrate cooling period before low-temperature growth begins and may subsequently be incorporated once growth resumes, effectively δ doping the sample. In the 400 °C-grown sample, grown on the same day and with the same Mn cell temperature, this effective δ doping does not occur, exemplifying the strong temperature dependence of Mn solubility in GaAs. Another possible explanation for this peak is that background impurities, such as oxygen, may be incorporated during the long growth pause, leading to a change in the SIMS ionization yield. This explanation is supported by the fact that the Al signal also shows a change in intensity at this same region even though the Al concentration should be constant.

C. Effective managanese concentration

Since we probe carrier spin splittings at the band edges of the QWs, then the presence of Mn in the AlGaAs barriers does not directly interfere with our measurements. The leakage of Mn into the barriers, however, makes the determination of the effective Mn concentration in the QWs nontrivial. Since we are primarily interested in the measurement of the conduction-band exchange parameter, we define the effective Mn concentration (Mn) in the QWs as the average of the SIMS concentration profile $Mn(z)$ weighted by the electron probability density along the growth axis $\rho_e(z)$. $\rho_e(z)$ is the square modulus of the ground-state electron wave function calculated using a one-dimensional Poisson-Schrödinger solver.[30] Thus, we calculate $Mn=\int Mn(z)\rho_e(z)dz$ by numerical integration. Mn and the corresponding values of x are listed for a variety of QWs in Table I. These values of x are then used in the extraction of $N_0\alpha$ from time-resolved KR measurements.[20]

As discussed previously, the decay of the Mn profiles on the substrate side of the QW is due to the knock-on effect, which is an artifact of the SIMS measurement. Therefore, the calculation of x as discussed above contains this error. We estimate the uncertainty of x by calculating the effective concentration assuming that the Mn profile on the substrate side of the QW is atomically sharp. Thus two values of x are calculated for each sample from which we calculate a standard deviation in x. These errors are generally $<3\%$, except for the $d=3$ nm QW set in which the error reaches 15%. The x errors lead to variations in our calculation of the s-d exchange parameter, which are included in the error bars of these parameters (Sec. VI).

D. Manganese incorporation versus well thickness

As discussed above, the Mn incorporation behavior in QWs is nontrivial, showing a peak in its concentration profile above the center of the well and a strong dependence on substrate temperature. Under these circumstances, we expect a strong variation of the incorporation of Mn for wells of different widths under fixed Mn beam flux. The Mn concentration (x) is plotted in Fig. 3(a) for four QW sample sets of varying width as a function of the inverse Mn effusion cell temperature. For each sample set of fixed width, the Mn

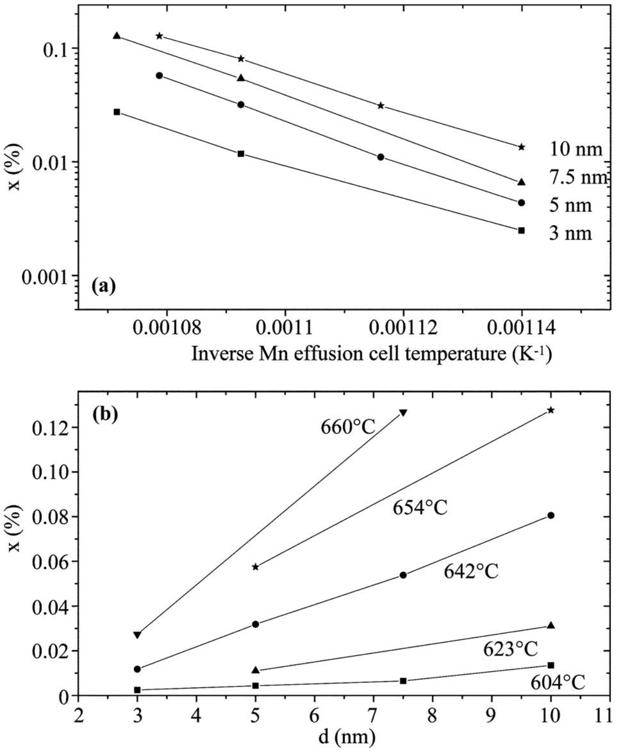

FIG. 3. (a) Percentage of x as calculated from SIMS data (see text) as a function of the inverse Mn effusion cell temperature. Four quantum well sample sets of different well width are shown. (b) Percentage of x versus quantum well width. Lines connect samples grown with the same Mn cell temperature, which is labeled in the figure.

concentration increases exponentially with Mn cell temperature, indicating a linear relation between the Mn beam flux and doping density. For any given Mn cell temperature, however, the doping density decreases with QW width. This trend is explicitly plotted in Fig. 3(b), where x within each quantum well is plotted as a function of quantum well width for various Mn cell temperatures. This plot demonstrates that Mn incorporation is a strong function of well thickness for the growth conditions used here, particularly for high Mn beam fluxes (high effusion cell temperatures).

The strong QW width dependence is likely due to the kinetics of Mn incorporation. These results are not surprising considering that many dopants do not immediately incorporate fully into semiconductors during MBE growth—e.g., In is well known to only fully incorporate into GaAs once a critical density of In is deposited on the surface[31]—for this reason sharp InGaAs/GaAs QWs are grown via predeposition of one monolayer of InAs followed by the alloy growth and subsequent reevaporation of the "In floating layer."[32] In this case, it is expected that narrow wells have lower total In densities than wider wells, which is what we observe in the case of the GaMnAs QWs.

IV. HALL EFFECT

Measurements of carrier concentration are carried out at $T=300$ K on samples prepared in the Van der Pauw geometry and results are shown in Table I. We examine carrier compensation related to As defects by comparing the electron density of a sample of 1 μm of n-GaAs (Si-doped $\sim 1 \times 10^{17}$ cm^{-3}) grown in typical high-temperature conditions (580 °C) to that of a sample with the identical structure but grown at 400 °C, the same temperature as used for the Mn-doped QWs. In the 400 °C-grown sample, the electron density is lower than in the 580 °C-grown sample by 1.1×10^{16} cm^{-3}, which provides an estimate for the compensation due to non-Mn-related growth defects—i.e., excess As. Si incorporation is amphoteric which can lead to both n and p doping (Si self-compensation); however, for high-temperature growth with Si-doping level less than 5×10^{18} cm^{-3}, we expect only n-type doping from Si.[33] At lower temperature, Si may also act as an acceptor;[34] thus, compensation assumed to be due to As defects could actually be occurring due to Si self-compensation, leading to an overestimate of excess As. For this reason, the carrier compensation we observe in the 400 °C-grown sample serves as an upper limit on the amount of excess As in our samples, $<1 \times 10^{16}$ cm^{-3}, which is drastically smaller than the typical concentrations measured in low-temperature (250 °C) grown GaAs, $\sim 1 \times 10^{20}$ cm^{-3}.[35] We also note that the compensation threshold for our samples is lower than for ALE-grown n-GaAs, 2×10^{18} cm^{-3}.[17]

A. Manganese hole-doping calibration

Given, as discussed above, that growth defects not related to Mn doping have a limited effect on the electronic properties for the chosen growth conditions, then the hole density in Mn-doped samples will be limited, for all practical purposes, only by the incorporation behavior of Mn. In order to determine the nature of Mn incorporation in our samples we investigate the p-doping dependence on Mn flux in a bulk calibration sample series grown under the same conditions as the Mn-doped QWs ($T_{sub}=400$ °C). These samples consist of 1 μm of GaAs doped with Mn at various effusion cell temperatures. We plot sheet concentration of holes (p2D) per hour of Mn shutter time as a function of the inverse temperature of the Mn effusion cell in these samples (Fig. 4). The doping rate demonstrates exponential thermal activation, fitting well to an Arrhenius equation, which indicates that there is a linear relation between the Mn beam flux and the hole density. Thus, for this doping range and under these growth conditions, Mn incorporation is mostly substitutional. The hole densities for two additional sample sets, 15-nm and 30-nm GaMnAs QWs, are plotted in Fig. 4. Arrhenius fits to these data match the fit for the bulk sample set, which indicates that Mn_{Ga} incorporation is sustained at these higher doping levels regardless of heterostructure effects. This is surprising considering that the effects of Mn penetration into the QW barriers and surface depletion could modify electrical properties, particularly for the narrower wells. The three-dimensional hole concentration (p) to Mn ratio, p/Mn, is listed in Table I. A fruitful comparison of these values to those in typical GaMnAs ($x>1\%$ and $T_{sub}=250$ °C) is difficult since GaMnAs usually contains orders of magnitude higher Mn and As defect concentrations than the samples discussed here.

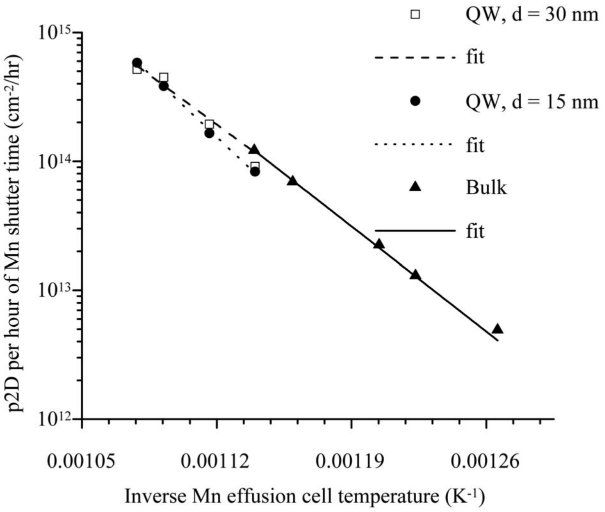

FIG. 4. The room-temperature two-dimensional hole density (p2D) per hour (h) of Mn shutter time as a function the inverse Mn source temperature. Three sample sets grown at 400 °C are plotted, and the data are fit to an exponential thermal activation (Arrhenius) equation, plotted as a line.

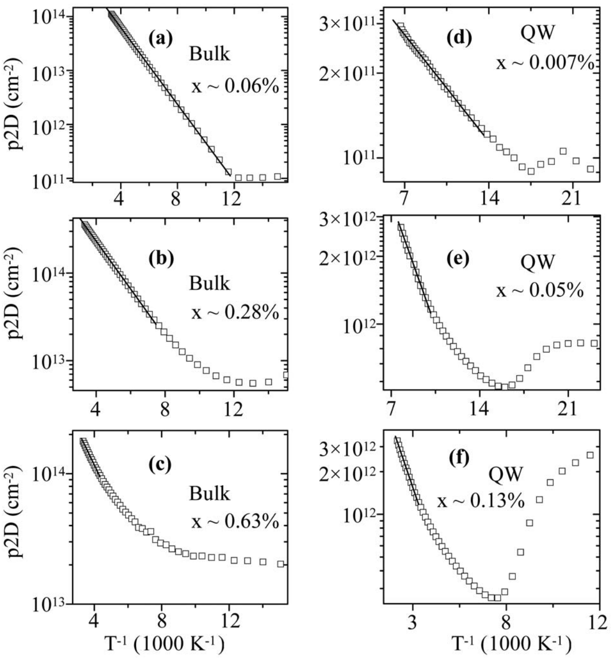

FIG. 5. The two-dimensional hole density (p2D) as a function of inverse sample temperature for 500-nm-thick bulk GaMnAs (a)–(c) and for 7.5-nm-thick GaMnAs QWs (d)–(f). Exponential thermal activation (Arrhenius) fits are plotted as lines over the temperature range used for fitting.

B. Manganese hole activation energy

In Fig. 5, the inverse sample temperature dependences of p2D for a sample set of 500-nm-thick layers of bulk GaMnAs and for a sample set of 7.5-nm-thick GaMnAs QWs are shown. At higher sample temperatures the activation energy (E_a) for holes is extracted from the linear portion of these plots, where the Mn-doped holes demonstrate clear exponential (Arrhenius) thermal activation. The Arrhenius behavior is maintained over a larger temperature range in the bulk than in the QWs, while at low temperature, carriers freeze out in both samples. In both bulk and QW samples, the linear portion of these plots decreases as the Mn concentration increases. Note that the linear fits to the data are carried out over smaller temperature ranges as x increases. This behavior is expected to originate from the formation and broadening of the Mn acceptor band for large doping levels.

In Fig. 6, the activation energies for a number of bulk and QW samples are plotted as a function of Mn concentration. For all samples measured, we have observed an activation energy lower than the 110 meV reported in the literature for an isolated Mn_{Ga} in GaAs.[36] This behavior was first observed in Mn-doped GaAs by Blakemore *et al.* where the thermal activation energy of Mn acceptors was found to be below the optical ionization energy of 110 meV.[37,38] The activation energies were lower than predicted due to impurity band broadening, suggesting a low-energy pathway due to sample inhomogeneity. In the case of impurity band formation, we would expect a continued lowering of the activation energy with increased Mn doping as the Mn acceptor level broadens into an impurity band and eventually merges with the GaAs valence band above the insulator-to-metal transition. For our bulk GaMnAs samples, the activation energy does decrease with increased Mn doping, but for QWs this effect is perhaps masked by a strong variation of the temperature-dependent hole concentration on QW width. For 3-nm-wide QWs, reliable activation energy for holes could not be extracted since either p2D is not linear over any significant temperature range or the Hall data are too noisy to be reliable. This behavior is also observed for the 5-nm-wide QWs in which E_a is only extracted for the two highest doping levels, but is not reliable for the two lowest Mn doped samples, whereas E_a is reliably measured in all the 7.5-nm, 10-nm, and bulk 500-nm samples. The dependence on well thickness is probably due to carrier compensation from impurities, such as oxygen,

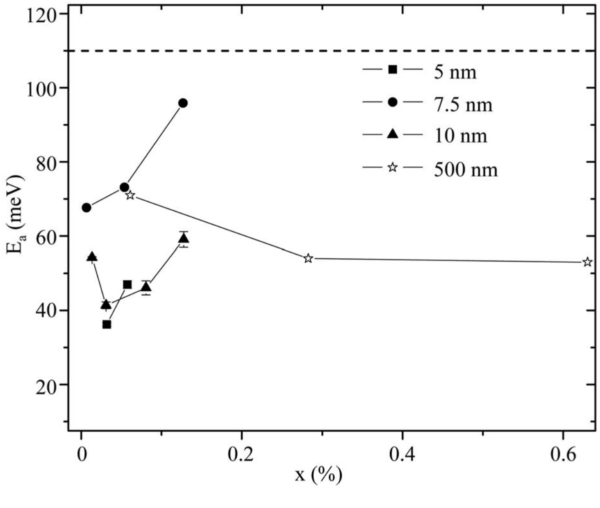

FIG. 6. The activation energy (E_a) for holes as a function of Mn concentration in bulk and QW samples extracted from Arrhenius fits—e.g., Fig. 5. The 110-meV activation energy for an isolated Mn^{2+} ion in GaAs is plotted as a dashed line for reference.

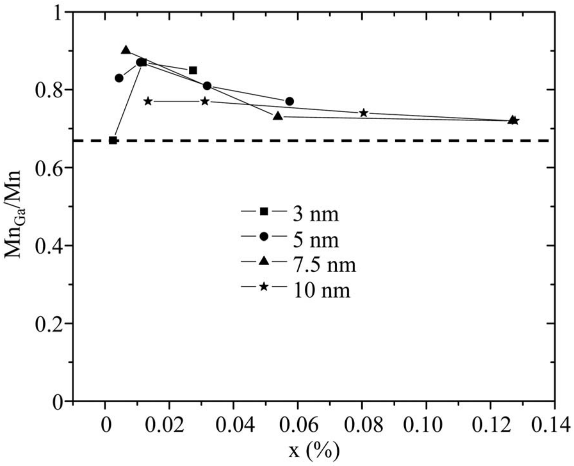

FIG. 7. The fraction of substitutional Mn (Mn_{Ga}/Mn) as a function of x, estimated assuming no surface depletion and full thermal activation of both Mn_{Ga}-doped holes and Mn_i-doped electrons. The minimum fraction of substitutional Mn (dashed line, 2/3) for p-type GaMnAs is plotted.

which are gettered by Al during the growth of the AlGaAs QW barriers, discussed previously (see Sec. III B). Barrier wave function penetration, and therefore barrier defect compensation, increases as the well width decreases.

V. SUBSTITUTIONAL MANGANESE INCORPORATION

An estimate of the fraction of Mn which is substitutionally incorporated can be made by assuming that each Mn_{Ga} donates one free hole and each Mn_i compensates two holes.[39] This calculation has recently been used in ferromagnetic GaMnAs ($x \sim 1\%$) to estimate the concentrations of Mn_i and Mn_{Ga} with respect to the crystal structure.[40] Here we ignore As defect compensation since it is negligible under our chosen growth conditions ($<1\times10^{16}$ cm^{-3}). We also assume that charge compensation due to Mn defects other than Mn_i (e.g., MnAs precipitates) are negligible. Thus, we write

$$p = Mn_{Ga} - 2Mn_i, \tag{1}$$

where Mn_{Ga} is the concentration of substitutional Mn and Mn_i is the concentration of interstitial Mn. Since Mn is the sum of Mn_{Ga} and Mn_i, then we rewrite Eq. (1) in terms of Mn_{Ga}/Mn,

$$Mn_{Ga}/Mn = \frac{1}{3}(p/Mn) + \frac{2}{3}. \tag{2}$$

Values of this ratio are provided for each sample in Table I and plotted for four QW sample sets of varying doping density in Fig. 7. The observation of hole conduction in all Mn-doped QWs provides a minimum value of $Mn_{Ga}/Mn=2/3$, while the real value is expected to be larger since Eq. (1) ignores holes which cannot be measured due to the incomplete thermal activation of impurity bound holes at 300 K or surface depletion. For increased Mn doping, the Mn_{Ga}/Mn ratio decreases, indicating that incorporation of growth defects, Mn_i or Mn containing second phases such as MnAs, is becoming significant. Precipitates remove Mn from the lattice, leading to a reduction in hole concentration relative to the purely substitutional case. Other forms of hole compensation such as interstitial-substitutional pairs[41] and dimers of two nearest-neighbor substitutional Mn (Ref. 42) are unlikely to be present in our samples due to the low doping concentrations. Optical signals, predominantly PL, show a similar degradation with increased Mn (see Secs. VI and VII). Note also, as indicated by the temperature dependence of the hole concentration, that particularly in the narrow QWs, $d=3$ and 5 nm compensation of holes due to barrier defects may also deflate our estimate of Mn_{Ga}/Mn. Despite these factors the fraction of Mn_{Ga} in all our samples is approximately 70%–90% as shown in Fig. 7.

VI. TIME-RESOLVED KERR ROTATION

This section describes in greater depth the experiments in Ref. 20. Electron spin dynamics are measured by time-resolved KR with the optical axis perpendicular to the applied magnetic field B (Voigt geometry) and parallel to the growth direction $\hat{z}$. The measurement, which monitors small rotations in the linear polarization of laser light reflected off of the sample, is sensitive to the spin polarization of electrons in the conduction band of the QW.[15] A mode-locked Ti:sapphire laser with a 76-MHz repetition rate and 250-fs pulse width tuned to a laser energy E_L near the QW absorption energy is split into a pump (probe) beam with an average power of 2 mW (0.1 mW). The helicity of the pump beam polarization is modulated at 40 kHz by a photoelastic modulator, while the intensity of the linearly polarized probe beam is modulated by an optical chopper at 1 kHz for lock-in detection. Both beams are focused to an overlapping 50-μm-diam spot on the sample which is mounted within a magneto-optical cryostat. The time delay Δt between pump and probe pulses is controlled using a mechanical delay line. The pump injects electron spins polarized perpendicular to B into the conduction band of the QW. The change in the probe polarization angle, $\theta_K(\Delta t)$, is proportional to the average electron spin polarization in the QW and is well fit to a single decaying cosine $\theta_K(\Delta t)=\theta_{\perp}e^{-\Delta t/T_2^*}\cos(2\pi\nu_L\Delta t+\phi)$, where $\theta_{\perp}$ is proportional to the total spin injected, T_2^* is the inhomogeneous transverse spin lifetime, ν_L is the electron spin precession (Larmor) frequency, and ϕ is the phase offset. No evidence of Mn^{2+} spin precession, which occurs in II-VI magnetically doped QWs,[15] has been observed in the samples studied here. The order of magnitude smaller x in our III-V QWs compared to the II-VI QWs puts any Mn^{2+} spin precession signal below the experimental detection limit.

Figure 8(a) shows typical time-resolved KR data measured at $B=8$ T for a Mn-doped QW ($d=7.5$ nm and $x \sim 0.05\%$) together with fit, as described above, demonstrating electron spin coherence in the GaMnAs system. KR data showing electron spin precession was observed to quench in all samples for $x>0.13\%$.

A. Transverse electron spin lifetime

The transverse electron spin lifetime (T_2^*) is plotted in Fig. 9 as a function of the percentage of Mn for all four QW

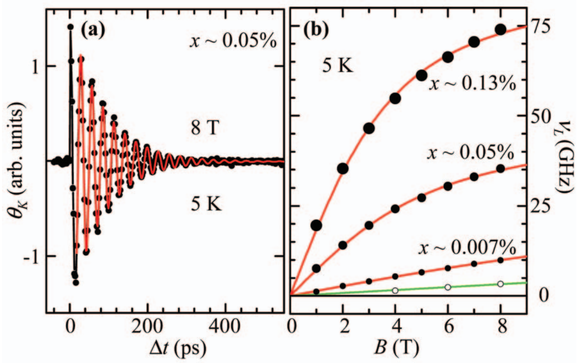

FIG. 8. (Color) Time-resolved electron spin dynamics in d =7.5 nm GaMnAs QWs. (a) An example of KR data (points) together with fit (line). (b) ν_L as a function of B for different x values (solid points); larger points indicate increasing x. Open data points are for the x=0 sample. Red lines in (b) are fits to Eq. (4).

sample sets. In all samples measured, we observe an increase in T_2^* with Mn doping as compared to the undoped control samples. This increase is consistent with the D'Yakonov-Perel (DP) spin relaxation mechanism since increasing impurity concentration makes the process of motional narrowing more efficient by providing additional momentum scatters.[43] After reaching a maximum at very low Mn doping ($x \sim 0.01\%$), T_2^* drops off as a function of x as shown in Fig. 9. This behavior suggests that for $x > 0.01\%$, the DP mechanism is no longer dominant. In this regime either the Elliot-Yafet (EY) or the Bir-Aronov-Pikus (BAP) relaxation mechanisms may limit conduction electron spin lifetimes, since both should increase in strength with increasing x.[44] EY relaxation, due to the spin-orbit interaction, grows stronger with larger impurity concentration, while the BAP process, based on the electron-hole exchange interaction, increases with increasing hole doping.

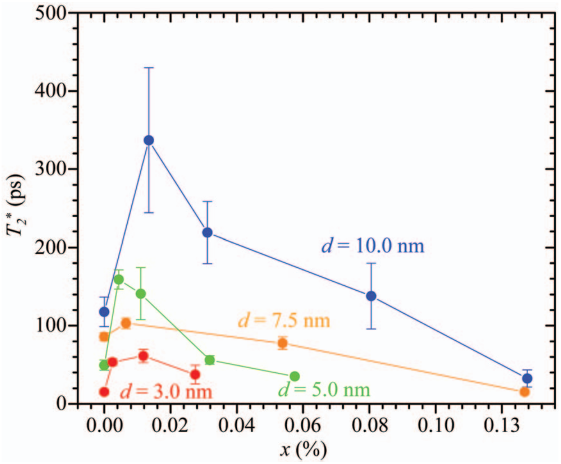

FIG. 9. (Color) The transverse electron spin lifetime (T_2^*) at T =5 K versus the percentage of Mn for four quantum well sample sets of varies width. The plotted values of T_2^* are the mean values from 0 to 8 T, and the error bars represent the standard deviations.

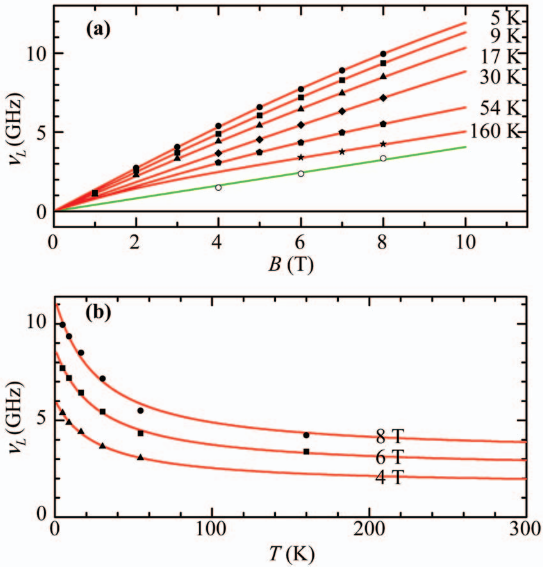

FIG. 10. (Color) Temperature dependence of ν_L for 7.5-nm quantum wells. (a) The effect of increasing T on the B dependence of ν_L for the sample with $x \sim 0.007\%$ (solid points) and for the x =0 sample (open points). (b) T dependence of ν_L at constant B for the $x \sim 0.007\%$ sample. Red lines in (a) and (b) are fits to Eq. (4).

In this discussion we have so far ignored the effects of the s-d exchange interaction on the electron spin relaxation process. In II-VI DMS, the presence of magnetic impurities leads to large relaxation rates, limiting the conduction electron spin lifetime.[15] Magnetic impurity doping in these materials results in relaxation through spin-flip scattering arising from the s-d exchange interaction. While the samples discussed in this report have s-d exchange energies which are several orders of magnitude smaller than in typical II-VI DMS, the effect of magnetic interactions on T_2^* cannot be totally ruled out. Several experiments can be carried out in order to examine the role of exchange interactions in the decoherence of electron spin including a finer dependence of T_2^* on x and a dependence on the temperature. A detailed study of changes in T_2^* as a function of QW width also may discern between the DP and the exchange scattering mechanism.[45] Such detailed studies will be the subject of future work. Finally we note that a qualitatively similar de-

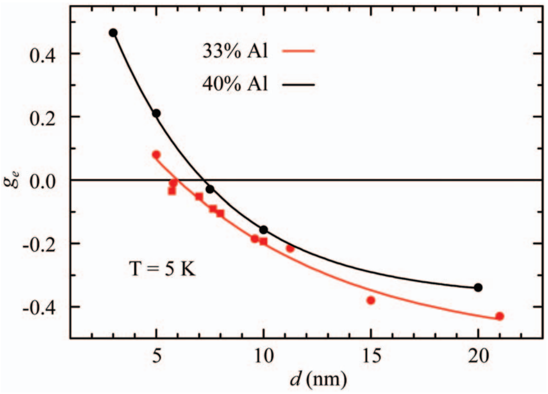

FIG. 11. (Color) g_e as a function of d. Black points are from control (x=0) samples of this study; red circles and squares are from Refs. 6 and 12, respectively. Lines guide the eye.

pendence of T_2^* on Mn doping as shown in Fig. 9 has recently been observed in InGaMnAs/GaAs QWs.[19]

B. Larmor precession frequency

ν_L is proportional to the total conduction-band spin splitting between spin-up and spin-down electrons ($\Delta E = E\uparrow - E\downarrow$) and can be expressed in terms of the Zeeman splitting (ΔE_g) and the *s*-*d* exchange splitting ($\Delta E_{s\text{-}d}$):

$$h\nu_L = \Delta E = \Delta E_g + \Delta E_{s\text{-}d} = g_e\mu_B B - xN_0\alpha\langle S_x\rangle. \qquad (3)$$

Here h is Planck's constant, g_e is the in-plane electron g factor, μ_B is the Bohr magneton, and $\langle S_x\rangle$ is the component of Mn^{2+} spin along B. $\langle S_x\rangle = -\frac{5}{2}B_{5/2}[5g_{Mn}\mu_B B/2k_B(T-\theta_P)]$, where $B_{5/2}$ is the spin-5/2 Brillouin function, g_{Mn} is the g factor for Mn^{2+}, k_B is Boltzmann's constant, and θ_P is the paramagnetic Curie temperature. Note that since the g factor for $\mathrm{Mn}^{2+}(g_{Mn}=2)$ is positive, for $B>0$, then $\langle S_x\rangle < 0$. We emphasize that a measurement of ν_L alone, because of phase ambiguity, does not determine the sign of ΔE.

In Fig. 8(b), ν_L is plotted as a function of B for a set of four samples with $d=7.5$ nm and varying x. The nonmagnetic ($x=0$) sample shows a linear field dependence of ν_L, from which we extract values of g_e as described in Eq. (3). As the Mn-doping concentration is increased, ν_L increases and its B dependence becomes nonlinear. Further, this field dependence shows the same Brillouin function behavior that is expected for the magnetization of paramagnetic GaMnAs, Eq. (3). The dependence of ν_L on B and T for the sample with $d=7.5$ nm and $x\sim 0.007\%$ is plotted in Fig. 10(a) and 10(b) together with values for the control sample, $x=0$ and $d=7.5$ nm. For the magnetic sample, as T is increased, ν_L decreases asymptotically toward the control sample value $g_e\mu_B B/h$ without crossing zero [Fig. 10(a)]. Thus, it follows from Eq. (3) and from the sign of $\langle S_x\rangle$ that for $d=7.5$ nm, $N_0\alpha$ has the same sign as g_e. For $d=7.5$ nm, $g_e<0$,[6] and thus $N_0\alpha<0$. This conclusion is also supported by the QW width dependence discussed below.

Using g_e extracted from the $x=0$ sample (green line) and Eq. (3) we fit ν_L data as a function of B and T to

$$\nu_L = \frac{g_e\mu_B B}{h} + \frac{5A}{2h}B_{5/2}\left(\frac{5\mu_B B}{k_B(T-\theta_P)}\right), \qquad (4)$$

which has only two fit parameters A and θ_P. Comparing Eq. (4) to Eq. (3), it is clear that $A = xN_0\alpha$. The data in Figs. 8(b) and 10 are fit to Eq. (4), with fits shown as red lines. A large negative θ_P (−24 K) is extracted from the fits for the sample with the lowest Mn doping (Fig. 10), which may be explained by an increased spin temperature of Mn^{2+} due to photoexcitation. This effect has been reported in II-VI DMS for low magnetic doping levels.[46] Also supporting this hypothesis, we find smaller values of $|\theta_P|$ (<7 K) in samples with larger x.

$N_0\alpha$ is examined in detail for QWs of varying d. For this analysis, we examine four sets of samples with various x (including $x=0$) for $d=3$, 5, 7.5, and 10 nm. Note that each sample set of constant d was grown on the same day, which we have observed to reduce QW thickness variations between samples within each set from $\sim 3\%$ to $<1\%$. Variations in QW thickness can affect the electron g factor and therefore result in errors in the determination of $xN_0\alpha$. By growing samples on the same day, the error in the determination of $xN_0\alpha$ is reduced from 10% to less than 3% as compared with samples grown on different days. In Fig. 11, g_e in the nonmagnetic ($x=0$) QWs is plotted as a function of d together with data from two other publications.[6,12] Our data track the thickness dependence of the QW g factor as previously reported with a slight positive shift in g_e. The larger Al concentration (40%) in the QW barriers used in our samples versus the concentration (33%) used in Refs. 6 and 12 accounts for this discrepancy.[47] Knowing the absolute sign of g_e for QWs of any width, we determine the sign of $N_0\alpha$ for each d in the manner described previously. With a calibrated sign, $\Delta E = h\nu_L$ is plotted in Fig. 12 as a function of B for all four QW sample sets with varying d. As shown in Fig. 12, for any given d, ΔE decreases as x increases. Following from Eq. (3) and from the sign of $\langle S_x\rangle$, this demonstrates that $N_0\alpha$ is negative—i.e., antiferromagnetic—which has been reproduced unambiguously in over 20 additional samples. A negative $N_0\alpha$ has also been measured in recent time-resolved FR measurements in InGaMnAs/GaAs QWs.[19]

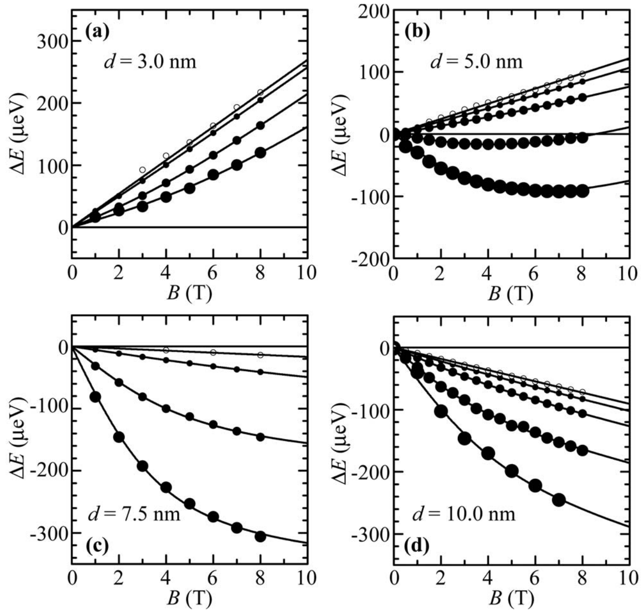

FIG. 12. ΔE as a function of B at $T=5$ K for QWs with (solid circles) and without Mn doping (open circles); larger points indicate increasing x. Fits to Eq. (4) are shown as lines.

The effect of increasing temperature on the B dependence of ΔE for the $d=5$ nm and $x\sim 0.032\%$ sample is shown in Fig. 13, which dramatically illustrates the negative *s*-*d* constant. For $d=5$ nm, g_e is weakly positive; thus, for $B>0$ and at high temperature, $\Delta E>0$. As the temperature decreases, $\Delta E_{s\text{-}d}$ becomes more negative as the paramagnetic susceptibility increases. At $T=10$ K and $B=7$ T, $\Delta E=0$ since the *s*-*d* exchange splitting is equal and opposite to the Zeeman splitting. For lower temperature, $\Delta E<0$ since $|\Delta E_{s\text{-}d}| > |\Delta E_g|$. We note that the data are well fit to Eq. (4) despite their highly nonlinear nature. We contrast our observation of antiferromagnetic *s*-*d* exchange in III-V GaMnAs,

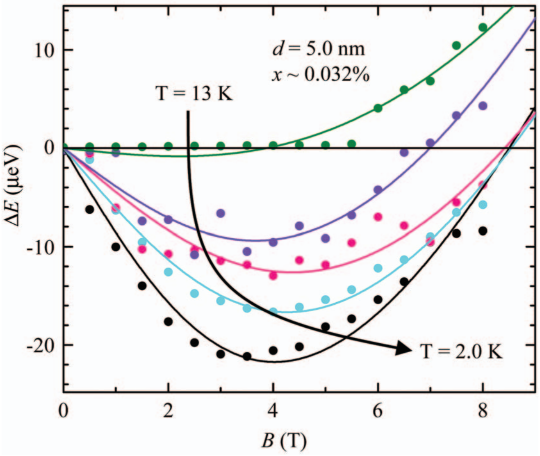

FIG. 13. (Color) ΔE for the sample with $d = 5$ nm and $x \sim 0.032\%$ at various temperatures. Fits to Eq. (4) are shown as lines.

with the ferromagnetic *s*-*d* exchange ubiquitous in II-VI DMS. In those systems symmetry forbids hybridization of *s* and *d* orbitals, such that only direct (ferromagnetic) *s*-*d* exchange is possible.[48] The antiferromagnetic *s*-*d* exchange in GaMnAs may be due to the narrower band gap of this material compared with II-VI, such that the conduction band has partial *p* character, thus allowing hybridization with the *d* orbitals localized on the Mn^{2+} impurities.

In Fig. 14, the fit parameter $A = xN_0\alpha$ is plotted as a function of x together with linear fits for each sample set of constant d. The finite values of $xN_0\alpha$ at $x=0$, extrapolated from the linear fits, are attributed to either the experimental error in the determination of g_e in the nonmagnetic QWs or error in the measurement of x, both of which have a negligible effect on the slope. These linear fits demonstrate that $N_0\alpha$ is constant over the measured doping range for QWs with the same width, but it varies with d as plotted in Fig. 15(a). $N_0\alpha$ is more negative the narrower the QW, while it appears to saturate for wide QWs. In II-VI DMS QWs, a negative change in $N_0\alpha$ as large as -170 meV was previously reported for increasing confinement and was attributed to a kinetic exchange coupling due to the admixture of valence- and conduction-band wave functions.[49]

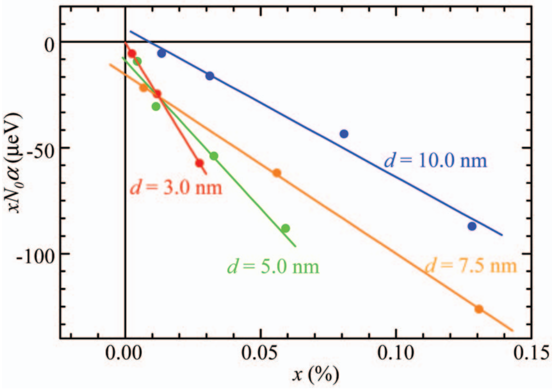

FIG. 14. (Color) $xN_0\alpha$ as a function of x from fits shown in Fig. 12; error bars are the size of the points. Linear fits are shown for each sample set of constant d.

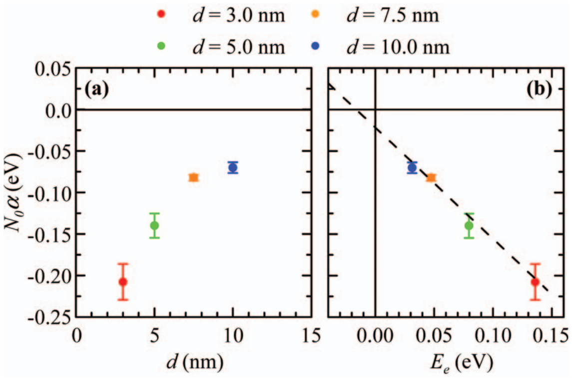

FIG. 15. (Color) The effect of confinement on *s*-*d* exchange coupling. (a) $N_0\alpha$ extracted from fits in Fig. 14 and plotted as a function of d. (b) $N_0\alpha$ as a function of electron kinetic energy for GaMnAs.

We plot $N_0\alpha$ as a function of the electron kinetic energy (E_e) in Fig. 15(b), and the data are linear. Here, E_e is defined as the energy between the bottom of the conduction band in the GaAs QW and the ground-state energy, which is calculated using a one-dimensional Poisson-Schrödinger solver and the material and structural parameters of the QWs.[25] Extrapolating to $E_e=0$ we obtain a bulk value of $N_0\alpha = -23 \pm 8$ meV for GaMnAs. A change in $N_0\alpha$ as large as -185 meV is observed in the narrowest wells measured ($d = 3$ nm), and the slope of $N_0\alpha(E_e)$ is roughly the same as reported by Merkulov *et al.* in II-VI DMS. Since $N_0\alpha > 0$ in bulk II-VI DMS, the kinetic exchange effect appears as a reduction of $|N_0\alpha|$ and is expected to cross through zero for very large confinement. Rather than a reduction, we observe an increase in $|N_0\alpha|$ in GaMnAs QWs. This observation is consistent with the predicted negative contribution of the kinetic exchange, since we measure $N_0\alpha < 0$ in our samples.

θ_P is observed to be negative for all the samples studied here, indicating that either long-range Mn-Mn coupling is antiferromagnetic or the Mn^{2+} spin temperature is larger than the lattice temperature. Preliminary studies on modulation *p*-doped structures indicate that the negative θ_P is due to a

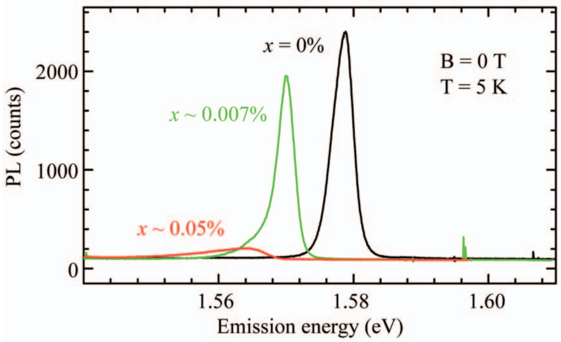

FIG. 16. (Color) PL plotted as a function of emission energy for a set of 7.5-nm QWs with varying Mn doping; the samples are excited with 1 W/cm^2 at 1.722 eV. Samples with $x > 0.13\%$ showed no PL.

combination of Mn^{2+} spin heating by photoexcitation, as previously discussed, and the lack of strong hole-mediated ferromagnetic Mn-Mn interaction, which occurs for much larger x. In our samples the mean Mn-Mn distance may be too long for hole-spin coherence to be maintained, thus precluding long-range ferromagnetic coupling.

Note that the magnetization of the Mn acceptors depends on their electronic structure. Mn acceptors in GaAs can exist in either the ionized $3d^5$ (Mn^{2+}) configuration A^- such that $g=2$ and $S=5/2$ or as a neutral complex A^0 consisting of the same $3d^5$ core with a loosely bound $S=3/2$ hole antiferromagnetically coupled to it; for this entire complex, $g=2.77$ and $J=1$.[50] Though found in GaP,[51] the fully bound $3d^4$ state with $S=4/2$ has never been observed in GaAs. A^- and A^0 have different angular momentum states and thus give rise to different bulk magnetizations as measured with a superconducting quantum interference device (SQUID), for instance. The spin state of the core $3d^5$ electrons ($S=5/2$), however, remains unchanged. Since *s*-*d* exchange involves the interaction between *s* electrons in the conduction band and *d* electrons of the Mn ion, the value of $N_0\alpha$ should remain unchanged regardless of the presence of the loosely bound hole.[52] In contrast, *p*-*d* exchange is strongly modified by this hole. The presence of a loosely bound hole in the neutral complex opens a ferromagnetic exchange path whereas the ionized acceptor offers only antiferromagnetic channels. In the literature, such a dependence on the nature of the Mn acceptor core is offered as an explanation for the apparent sign flip of the *p*-*d* term as the Mn concentration was increased from the very dilute limit (paramagnetic) to the high-doping regime (ferromagnetic). It may also explain the widely varying values of $N_0\beta$ measured in our PL experiments (Sec. VII). We emphasize that our exchange splitting model takes $g_{Mn}=2$ and thus neglects any effect of the loosely bound hole on the core-state g factor since the exchange interaction between the hole and core is expected to be small.[53] Measurements in III-V DMS support this assumption by consistently showing $g_{Mn}=2.0$. Therefore, the relative concentration of A^- and A^0 centers in our samples should have a negligible effect on both $N_0\alpha$ and g_{Mn}, allowing us to ignore this detail in our extraction of $N_0\alpha$ from the data.

VII. PHOTOLUMINESCENCE

Since hole spin lifetimes are very short in GaAs QWs (<10 ps), we rely on measurements of PL to shed light on the *p*-like valence band and its magnetic coupling to Mn-bound *d* electrons, $N_0\beta$. In addition, because recombination happens near impurities, PL can reveal important information on defects and magnetic doping. Here we elaborate on experiments from Ref. 20 in more complexity. Polarization-resolved PL is measured as a function of B in the Faraday geometry with PL collected normal to the sample surface. The excitation laser is linearly polarized and focused to a spot 100 μm in diameter with an energy set above the QW absorption energy. While PL is seen to quench with increasing Mn doping, as seen in Fig. 16, QWs with $x=0$ or with small x emit PL whose energy dependence is well fit by two Gaussians (Fig. 17). The emission energy of the narrower, higher-energy Gaussian peak tracks the B dependence expected for the Zeeman splitting in QWs, indicating that this peak is due to heavy-hole–exciton recombination. On the other hand, the wider, lower-energy Gaussian is likely due to donor-bound exciton emission from shallow donors in the QWs. These shallow donors are likely Mn_i, since the emission linewidth increases as the calculated Mn_i concentration increases. Though the lower-energy Gaussian is the result of Mn doping, it is also present in some nonmagnetic samples grown with a cold Mn cell (Fig. 17), perhaps due to an impurity level of Mn_i ($\leqslant 10^{15}$ cm^{-3}).

In addition to quenching the PL, increased Mn doping broadens the low-energy emission peak. Figure 16 shows the zero-field PL emission at $T=5$ K for 7.5-nm-wide QWs of varying Mn doping. The effect of increasing Mn doping is qualitatively identical for all QWs of varying width: $d=3.0$, 5.0, 7.5, and 10.0 nm. As doping increases, the PL broadens in energy, redshifts, and decreases in intensity, eventually quenching. The decreasing intensity of the PL with increasing Mn doping parallels the degradation in KR signal with Mn doping. The degradation of these two optical signals, each with distinct physical origins—i.e., emission and absorption—reflects the increasing density of crystalline defects with Mn doping.

A. Zeeman splitting

The splitting in the polarized emission energy of the higher-energy Gaussian, $\Delta E_{PL}=E_{\sigma^+}-E_{\sigma^-}$, is measured in all the nonmagnetic samples. For small fields ($B<2$ T, ΔE_{PL} depends linearly on field with the slope giving the out-of-plane heavy-hole-exciton g factor (g_{ex}). The extracted values of g_{ex} agree within the experimental error with previously published values.[7] At higher fields, ΔE_{PL} deviates from linearity, particularly in the wider QWs as shown in Figs. 18(a) and 18(b) where it reverses sign in both the 10-nm and 7.5-nm QWs for $x=0$ at $|B|\sim 5$ T.

In Mn-doped samples, ΔE_{PL} results from both the Zeeman splitting (ΔE_{gex}) and the *sp*-*d* exchange splitting ($\Delta E_{sp\text{-}d}$):

$$\Delta E_{PL}=\Delta E_{gex}+\Delta E_{sp\text{-}d}=-g_{ex}\mu_B B+xN_0(\alpha-\beta)\langle S_x\rangle. \quad (5)$$

Using the measurements of g_{ex} from the $x=0$ samples and the previously extracted values of $\langle S_x\rangle$ and $N_0\alpha$ at $T=5$ K (Fig. 12), we fit ΔE_{PL} to Eq. (5). In the 10-nm QW for low fields we estimate $N_0\beta=-0.85\pm0.38$ eV using the fits shown in Fig. 18(a) as blue lines. As Fig. 18(a) makes clear, this model breaks down at high fields where nonlinearities dominate ΔE_{PL}.

Similar nonlinear behavior in ΔE_{PL} at high fields in the 7.5-nm QWs, as shown in Fig. 18(b), contributes to the large uncertainty in our estimates of $N_0\beta$. Further complicating the determination of $N_0\beta$ are the widely differing values extracted for samples of different widths. Using fits shown in Fig. 18, we find $N_0\beta=-2.9\pm1.5$, $+24.5\pm1.8$, and $+4.3\pm9.4$ eV for QWs with $d=7.5$, 5.0, and 3.0 nm, respectively. Such dissagreement between samples indicates the incompleteness of our model for the valence-band; the mixing of valence-band states may be contributing to the problem-

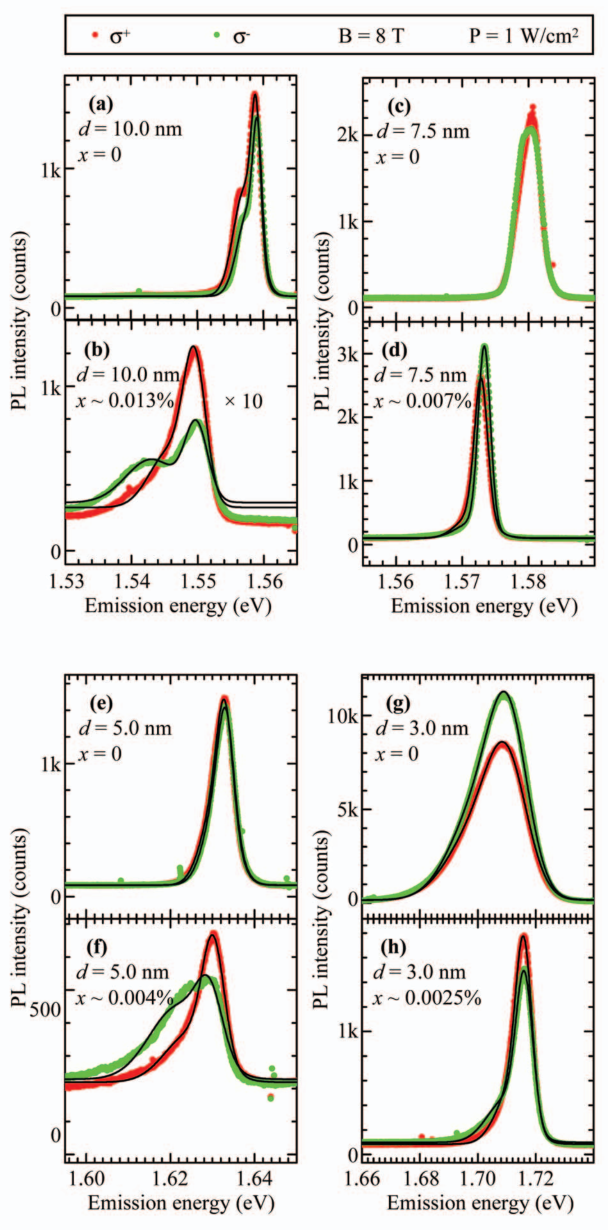

FIG. 17. (Color) Polarization-resolved PL for QWs of varying d and x at $T=5$ K. Two-Gaussian fits to the data are shown as black lines, and the higher-energy Gausssian is attributed to the heavy-hole exciton in the QW. The excitation enregy is set to 1.722 eV for (a)–(f) and 2.149 eV for (g) and (h).

atic extraction of the p-d exchange coupling especially for small d.[7] Clearly, more work is necessary for the determination of $N_0\beta$ in GaMnAs QWs and its dependence on d. Previous measurements in bulk GaMnAs provide little guidance, with one report suggesting positive p-d exchange for low x (paramagnetic) (Ref. 54) and others finding negative p-d exchange for much larger x (ferromagnetic) (Refs. 55–57).

B. Photoluminescence polarization

We compare the PL polarization spectra of the 7.5-nm QW with $x\sim0.007\%$ with the well-known Mn-acceptor emission line in bulk GaAs at 1.4 eV [Figs. 19(a) and 19(b)].[36] PL polarization is defined here as $(I_{\sigma+}-I_{\sigma-})/(I_{\sigma+}+I_{\sigma-})$. The bulk Mn-acceptor line, shown in Fig. 19(b), is measured in the same sample, resulting from the unintentional doping of Mn in the 300-nm GaAs buffer layer grown below the QW structure; the SIMS profiles in Fig. 1 show that the Mn concentration in this layer is less than 1×10^{16} cm^{-3}. The polarization of this peak demonstrates a paramagnetic (Brillouin function) field dependence, shown in Fig. 19(d), following the magnetization of the Mn$_{Ga}$ acceptors in the bulk GaAs. The low-energy peak in the QW PL polarization coincides with the low-energy PL peak which we assigned to emission from Mn$_i$-donor-bound excitons. Its polarization is plotted in Fig. 19(c) (solid points) and demonstrates similar paramagnetic (Brillouin function) behavior with field and temperature to that of the bulk Mn-acceptor line.

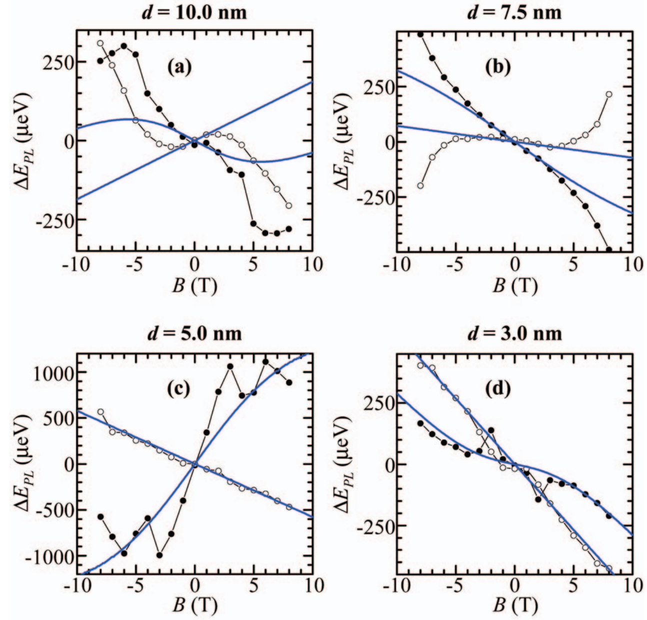

FIG. 18. (Color) Polarized emission splitting (ΔE_{PL}) as a function of B at $T=5$ K for QWs of varying d and x. Data from QWs with $x=0$ are shown as open circles, while data from QWs with $x\sim0.013\%$ in (a), $x\sim0.007\%$ in (b), $x\sim0.004\%$ in (c), and $x\sim0.0025\%$ in (d) are shown as solid circles. Fits to ΔE_{PL} for $|B|<2$ T appear as blue lines.

The polarization of the bulk Mn-acceptor line is proportional to the spin polarization of local Mn^{2+} moments since the PL from this line results from conduction-band electrons recombining with holes trapped on Mn$_{Ga}$ acceptors. The spin of these holes is coupled to the local Mn^{2+} spin.[58] We postulate a similar mechanism for the low-energy polarization feature in the QW PL in which holes in the valence band of the QW recombine with electrons bound to Mn$_i$ donors. The clear Brillouin-like field dependence indicates that the recombinant polarization originates around isolated paramagnetic Mn impurites in the lattice—i.e., either Mn$_{Ga}$ acceptors or Mn$_i$ donors. The Brillouin-like behavior is inconsistent

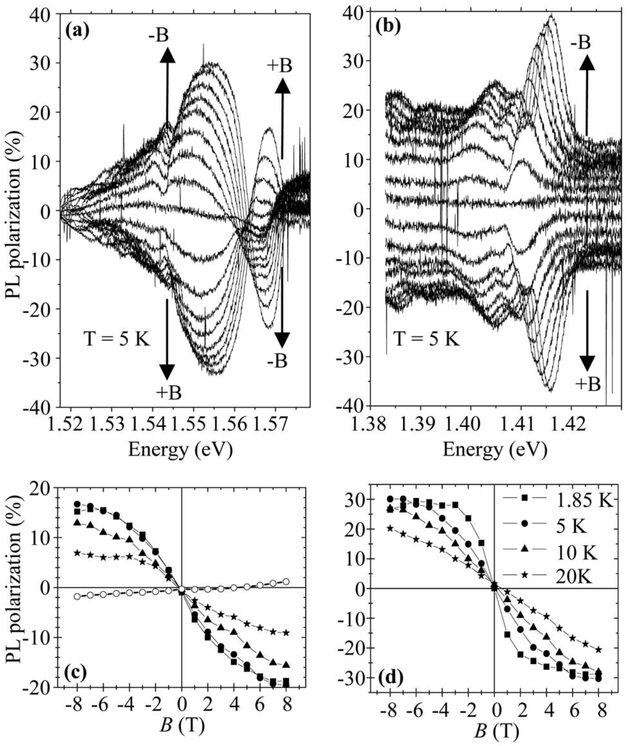

FIG. 19. PL polarization spectra for a 7.5-nm GaMnAs QW with an 1.72-eV excitation at 1.0 mW (a) near the QW emission peaks (~1.6 eV) and (b) at the bulk Mn-acceptor line for GaMnAs (~1.4 eV), which results from unintentional Mn doping in the 300-nm-thick GaAs buffer layer. The spectra are plotted as a function of emission energy for different magnetic fields from −8 to +8 T at 1-T intervals. (c) The PL polarization integrated over a single emission peak as a function of B for the high-energy (~1.57 eV at T=5 K, open circles) and low-energy (~1.55 eV at several temperatures, solid symbols) peaks and (d) for the bulk Mn-acceptor line peak plotted for several temperatures.

with coupled Mn centers such as interstitial-substitutional pairs, which couple antiferromagnetically and which are unlikely to be present in samples with such low Mn content.[41] The ~20-meV redshift of the polarization peak from the main QW peak does not match the 110-meV binding energy of the substitutional acceptor. While there is an excited state of the Mn_{Ga} acceptor with a binding energy of 26 meV,[59] recombination from this excited state is unlikely when each acceptor is filled with, at most, one hole and given that PL usually originates from the lowest available energy levels. Rather, we assume that the recombination originates from the Mn_i donor and the valance band in the QW. Comparison to the experimentally measured Mn_i donor binding energy is not possible since none are reported. The postulated coupling of the electron spin to Mn_i spin results in polarized emission which follows the magnetization of Mn_i within the QW. These measurements open the possibility of indirectly measuring the magnetization of the Mn impurities in the QWs using polarization-resolved magneto-PL.

The high-energy feature in the QW PL polarization involves recombination of electrons and holes bound to the QW, but delocalized relative to the Mn states. Due to the exchange interactions in both the valence and conduction bands, the spin splitting, and thus the resulting polarization, should have a Brillouin function field dependence, Eq. (5). For the small values of x studied here, however, these effects are not resolvable and the polarization shows a weaker field dependence, Fig. 19(c) (open points), with an opposite sign compared to the polarization of the low-energy peak (solid points).

VIII. CONCLUSIONS

In summary, we demonstrate the growth of III-V GaMnAs-based heterostructures in which coherent electron spin dynamics and PL can be observed. By lowering the substrate temperatures during growth, sharper Mn profiles and higher Mn concentrations are attained; however, optical signals eventually quench ($T_{sub} < 400\ ^\circ\mathrm{C}$) likely due to incorporation of defects by Al gettering, such as oxygen. Optical signals are also seen to quench for $x > 0.13\%$. Hole doping due to substitutional Mn incorporation is sensitive to the quantum well width, indicative of compensation by defects in the AlGaAs barriers. The activation energy of holes in the QWs is lower than for an isolated substitutional Mn in GaAs, providing evidence for impurity-band formation and broadening due to large Mn doping. The crystallographic incorporation behavior is estimated from the SIMS and Hall data, and we find that for all samples studied at least 70%–90% of Mn is located on substitutional Ga sites. The exchange-induced spin splitting in the conduction band in the GaMnAs QWs matches the traditional paramagnetic DMS picture and allows for the determination of the *s*-*d* exchange parameter via time-resolved electron spin spectroscopy. Surprisingly the measured *s*-*d* exchange coupling is antiferromagnetic in GaMnAs QWs,[20] a result not predicted by current DMS theories. No evidence of long-range Mn spin coupling is observed, but negative effective Curie temperatures indicate spin heating of the Mn sublattice by photoexcitation. Electron spin lifetimes in the QWs increase for the lowest Mn dopings compared with undoped samples, indicating the dominance of the Dyakanov-Perel mechanism over spin-flip scattering in this regime. The ability to magnetically dope III-V and maintain sensitive optical properties opens the door for more complex structures to be used in the study of both free carriers and magnetic ion spins at fast time scales, a technology which was previously limited to II-VI DMS.

ACKNOWLEDGMENTS

The authors thank T. Mates (MRL, UC Santa Barbara) and Charles Evans and Associates for SIMS measurements, J. H. English and A. W. Jackson for MBE technical assistance, and J. Miller (Smelrose Institute) for entertaining discussions. This work was financially supported by DARPA, ONR, and made use of MRL Central Facilities supported by the MRSEC Program of the National Science Foundation under Award No. DMR00-80034. One of us (N.P.S.) acknowledges the support of the Fannie and John Hertz Foundation.

[1] H. Ohno, A. Shen, F. Matsukura, A. Oiwa, A. Endo, S. Katsumoto, and Y. Iye, Appl. Phys. Lett. **69**, 363 (1996).
[2] T. Dietl, H. Ohno, and F. Matsukura, Phys. Rev. B **63**, 195205 (2001).
[3] H. Ohno, J. Magn. Magn. Mater. **272**, 1 (2004).
[4] A. H. Macdonald, P. Schiffer, and N. Samarth, Nat. Mater. **4**, 195 (2005).
[5] T. Dietl, in *Handbook of Semiconductors*, edited by S. Mahajan (North-Holland, Amsterdam, 1994), Vol. 3B, p. 1251.
[6] M. J. Snelling, G. P. Flinn, A. S. Plaut, R. T. Harley, A. C. Tropper, R. Eccleston, and C. C. Phillips, Phys. Rev. B **44**, 11345 (1991).
[7] M. J. Snelling, E. Blackwood, C. J. McDonagh, and R. T. Harley, Phys. Rev. B **45**, R3922 (1992).
[8] N. J. Traynor, R. T. Harley, and R. J. Warburton, Phys. Rev. B **51**, 7361 (1995).
[9] Y. K. Kato, R. C. Myers, A. C. Gossard, and D. D. Awschalom, Science **306**, 1910 (2004).
[10] G. Salis, Y. Kato, K. Ensslin, D. C. Driscoll, A. C. Gossard, and D. D. Awschalom, Nature (London) **414**, 619 (2001).
[11] Y. Kato, R. C. Myers, D. C. Driscoll, A. C. Gossard, and D. D. Awschalom, Science **299**, 1201 (2003).
[12] M. Poggio, G. M. Steeves, R. C. Myers, N. P. Stern, A. C. Gossard, and D. D. Awschalom, Phys. Rev. B **70**, 121305(R) (2004).
[13] Y. Kato, R. C. Myers, A. C. Gossard, and D. D. Awschalom, Nature (London) **427**, 50 (2004).
[14] Y. K. Kato, R. C. Myers, A. C. Gossard, and D. D. Awschalom, Phys. Rev. Lett. **93**, 176601 (2004).
[15] S. A. Crooker, D. D. Awschalom, J. J. Baumberg, F. Flack, and N. Samarth, Phys. Rev. B **56**, 7574 (1997); S. A. Crooker, J. J. Baumberg, F. Flack, N. Samarth, and D. D. Awschalom, Phys. Rev. Lett. **77**, 2814 (1996).
[16] R. C. Myers, K. C. Ku, X. Li, N. Samarth, and D. D. Awschalom, Phys. Rev. B **72**, 041302(R) (2005).
[17] E. Johnston-Halperin, J. A. Schuller, C. S. Gallinat, T. C. Kreutz, R. C. Myers, R. K. Kawakami, H. Knotz, A. C. Gossard, and D. D. Awschalom, Phys. Rev. B **68**, 165328 (2003).
[18] R. C. Myers, A. C. Gossard, and D. D. Awschalom, Phys. Rev. B **69**, 161305(R) (2004).
[19] R. C. Myers, N. P. Stern, M. Poggio, A. W. Jackson, A. C. Gossard, and D. D. Awschalom (unpublished).
[20] R. C. Myers, M. Poggio, N. P. Stern, A. C. Gossard, and D. D. Awschalom, Phys. Rev. Lett. **95**, 017204 (2005).
[21] K. Wagenhuber, H-P. Tranitz, M. Reinwald, and W. Wegscheider, Appl. Phys. Lett. **85**, 1190 (2004).
[22] C. A. Evans, Jr., Anal. Chem. **44**, 67A (1972).
[23] A. Benninghoven, Surf. Sci. **35**, 427 (1973).
[24] H. W. Werner and H. A. M. DeGrefte, Surf. Sci. **35**, 458 (1973).
[25] A. M. Nazmul, S. Sugahara, and M. Tanaka, J. Cryst. Growth **251**, 303 (2003).
[26] T. Ishitani and R. Shimizu, Appl. Phys. **6**, 241 (1975).
[27] T. Ishitani and R. Shimizu, Appl. Phys. **6**, 277 (1975).
[28] K. Akimoto, M. Kamada, K. Taira, M. Arai, and N. Watanabe, J. Appl. Phys. **59**, 2833 (1986).
[29] T. Achtnich, G. Burri, M. A. Py, and M. Ilegems, Appl. Phys. Lett. **50**, 1730 (1987).
[30] One-dimensional Poisson-Schrödinger solver written by G. Snider (http://www.nd.edu/gsnider/).
[31] H. Toyoshima, T. Niwa, J. Yamazaki, and A. Okamoto, Appl. Phys. Lett. **63**, 821 (1993).
[32] J. Nagle, J. P. Landesman, M. Larive, C. Mottet, and P. Bois, J. Cryst. Growth **127**, 550 (1993).
[33] J. Maguire, R. Murray, R. C. Newman, R. B. Beall, and J. J. Harris, Appl. Phys. Lett. **50**, 516 (1987).
[34] B. Grandidier, D. Stivenard, J. P. Nys, and X. Wallart, Appl. Phys. Lett. **72**, 2454 (1998).
[35] M. Missous and S. O'Hagan, J. Appl. Phys. **75**, 3396 (1994).
[36] P. W. Yu and Y. S. Park, J. Appl. Phys. **50**, 1097 (1979).
[37] J. S. Blakemore, Winfield J. Brown, Jr., Merrill L. Stass, and Dustin A. Woodbury, J. Appl. Phys. **44**, 3352 (1973).
[38] D. A. Woodbury and J. S. Blakemore, Phys. Rev. B **8**, 3803 (1973).
[39] S. C. Erwin and A. G. Petukhov, Phys. Rev. Lett. **89**, 227201 (2002).
[40] L. X. Zhao, C. R. Staddon, K. Y. Wang, K. W. Edmonds, R. P. Campion, B. L. Gallagher, and C. T. Foxon, Appl. Phys. Lett. **86**, 071902 (2005).
[41] K. M. Yu, W. Walukiewicz, T. Wojtowicz, I. Kuryliszyn, X. Liu, Y. Sasaki, and J. K. Furdyna, Phys. Rev. B **65**, 201303(R) (2002).
[42] H. Raebiger, A. Ayuela, and R. M. Nieminen, J. Phys.: Condens. Matter **16**, L457 (2004).
[43] J. Fabian and S. das Sarma, J. Vac. Sci. Technol. B **17**, 1708 (1999).
[44] *Optical Orientation, Modern Problems in Condensed Matter Science*, edited by F. Meier and B. P. Zachachrenya (North-Holland, Amsterdam, 1984), Vol. 8.
[45] Y. G. Semenov, Phys. Rev. B **67**, 115319 (2003).
[46] D. Keller, D. R. Yakovlev, B. Konig, W. Ossau, Th. Gruber, A. Waag, L. W. Molenkamp, and A. V. Scherbakov, Phys. Rev. B **65**, 035313 (2001).
[47] C. Weisbuch and C. Hermann, Phys. Rev. B **15**, 816 (1977).
[48] B. E. Larson, K. C. Hass, H. Ehrenreich, and A. E. Carlsson, Phys. Rev. B **37**, 4137 (1988).
[49] I. A. Merkulov, D. R. Yakovlev, A. Keller, W. Ossau, J. Heurts, A. Waag, G. Landwehr, G. Karczewski, T. Wojtowicz, and J. Kossut, Phys. Rev. Lett. **83**, 1431 (1999).
[50] J. Schneider, U. Kaufmann, W. Wilkening, M. Baeumler, and F. Kohl, Phys. Rev. Lett. **59**, 240 (1987).
[51] J. Kreisel, W. Ulrici, M. El-Metoui, A. M. Vasson, A. Vasson, and A. Gavaix, Phys. Rev. B **54**, 10508 (1996).
[52] J. Szczytko, W. Mac, A. Twardowski, F. Matsukura, and H. Ohno, Phys. Rev. B **59**, 12935 (1999).
[53] M. Linnarsson, E. Janzen, B. Monemar, M. Kleverman, and A. Thilderkvist, Phys. Rev. B **55**, 6938 (1997).
[54] J. Szczytko, W. Mac, A. Stachow, A. Twardowski, P. Becla, and J. Tworzydlo, Solid State Commun. **99**, 927 (1996).
[55] F. Matsukura, H. Ohno, A. Shen, and Y. Sugawara, Phys. Rev. B **57**, R2037 (1998).
[56] J. Okabayashi, A. Kimura, O. Rader, T. Mizokawa, A. Fujimori, T. Hayashi, and M. Tanaka, Phys. Rev. B **58**, R4211 (1998).
[57] M. A. Zudov, J. Kono, Y. H. Matsuda, T. Ikaida, N. Miura, H. Munekata, G. D. Sanders, Y. Sun, and C. J. Stanton, Phys. Rev. B **66**, 161307(R) (2002).
[58] A. Petrou, M. C. Smith, C. H. Perry, J. M. Worlock, J. Warnock, and R. L. Aggarwal, Solid State Commun. **55**, 865 (1985).
[59] B. Lakshmi, G. Favrot, and D. Heiman, Proc. SPIE **5359**, 290 (2004).